J Mol Model (2014) 20:2506
DOI 10.1007/s00894-014-2506-z

ORIGINAL PAPER

A computational study on the photoelectric properties of various Bi_2O_3 polymorphs as visible-light driven photocatalysts

Fang Wang · Kun Cao · Qian Zhang · Xuedong Gong · Ying Zhou

Received: 3 August 2014 / Accepted: 13 October 2014 / Published online: 9 November 2014

Abstract This paper presents first-principle studies on the photoelectric properties of various Bi_2O_3 polymorphs. The intrinsic reason of different photocatalytic activities was revealed by electronic structures and optical features. Results showed that for α, β, and γ-Bi_2O_3, the top of valence bands were mainly constructed by Bi6s and O2p orbitals, and the bottom of conduction bands were dominantly composed by Bi6p orbital. However, two intermediate bands were found at the Fermi level for γ-Bi_2O_3, which leads to a two-step transition from the top of valence band to the bottom of conduction band and facilitates electron transition under irradiation. Absent forbidden gap was found in δ-Bi_2O_3, resulting in a semimetallic character due to its intrinsic oxygen vacancy and high ionic conductivity. Moreover, the optical properties of α, β, and γ-Bi_2O_3 were investigated by absorption spectrum, dielectric constant function, and energy loss spectroscopy. We concluded that the photocatalytic activities followed in the order of γ-Bi_2O_3>β-Bi_2O_3>α-Bi_2O_3, in accord with the experimental report. Calculation results illustrated the experimental observations and provided a useful guidance in exploring promising visible-light semiconductor photocatalysts.

Keywords Bismuth oxide · Electronic structure · First-principle calculation · Optical property

F. Wang (✉) · K. Cao · Q. Zhang · Y. Zhou
School of Material Science and Engineering,
Southwest Petroleum University, Chengdu 610500, China
e-mail: wangfnjust@163.com

X. Gong
Department of Chemistry, Nanjing University of Science and Technology, Nanjing 210094, China

Introduction

Semiconductor photocatalysts have received increasing attention because of their wide applications in the fields of environmental purification and solar energy conversion during the past decades [1–3]. Among the numerous photocatalysts, TiO_2 is known as an outstanding photocatalytic material owing to its good thermal stability, low cost, non-toxic, and high photocatalytic activity [4–6]. However, the wide band gaps (3.2 eV for anatase and 3.0 eV for rutile TiO_2) confine them to absorb only ultraviolet-light which accounts for approximate 4 % of solar power [7, 8] , Therefore, it is urgently needed to explore and synthesize more efficient visible-light driven photocatalysts [9, 10]. Recently, Bi_2O_3 has become the hot topic in the study of visible-light photocatalysts due to the unique crystal structure and electronic properties [11, 12].

Bismuth oxide exists in six crystalline polymorphs, α--(monoclinic), β-(tetragonal), γ-(based centered cubic), δ--(face centered cubic), ε-(orthorhombic), and ω-(triclinic) [13–18]. Among them, the former four polymorphs were reported most by experimental work. The α phase is stable at relatively low temperatures, δ phase is only stable at temperatures between 729 °C and 825 °C and a large hysteresis has been observed on cooling from high temperatures to room temperatures, with the possible occurrences of two intermediate metastable phases with β or γ phase [18]. Experimental studies showed that their relatively narrow band gaps varying from 2.1 to 2.8 eV extended the optical absorption to the visible-light region [19, 20]. Generally, Bi_2O_3 with different polymorphs exhibits different photocatalytic activity. Zou et al. [21] have prepared α,β, and γ-Bi_2O_3 by a chemical precipitation method and showed the photocatalytic performance follows in the sequence of γ>β>α in photodegrading RhB. Another work reported photocatalytic activity was in the order of β>α>δ [22]. To date, most previous studies were focused on the photocatalytic performance by experiments,

with few on the structural and photoelectric features which significantly determine their photocatalytic activity. Some theoretical studies have simulated the band structures of Bi_2O_3 via the density function theory (DFT) [22, 23]; however, the relationship between the photoelectric structures and the photocatalytic activity has not been well explicated to the best of our knowledge. Therefore, it is of fundamental importance to understand the role of electronic and optical properties in tuning the photocatalytic activities of Bi_2O_3. In this paper, we carried out first-principle calculations on the band structures, density of states, and optical properties based on the quantum mechanics theory, aiming at understanding the intrinsic features of various Bi_2O_3 polymorphs and providing theoretical explanation for related experimental study [12, 21].

Computational details

The first-principle calculations were performed at the generalized gradient approximation (GGA) functional of Perdew-Wang (PW91) level with the Vanderbilt-type ultrasoft pseudopotential and a plane-wave expansion of the wave functions implemented in the CASTEP package [24–27]. The valence atoms configurations are $6s^26p^3$ for Bi and $2s^22p^4$ for O. The geometry optimization of lattice parameters and internal coordinates was relaxed using Broyden, Fletcher, Goldfarb, and Shannon (BFGS) minimization technique [24]. Cutoff energy of 380 eV was used for plane-wave, and the Brillouin zone was separately sampled at 2×2×2 Monkhorst-Pack *k*-points for α, β, γ, and δ. In the geometry relaxation, the total energy of system was converged to less than 2×10^{-6} eV/atom, the residual force less than 0.01 eV/Å, and the displacement of atoms and residual bulk stress less than 0.002 Å and 0.1 GPa, respectively. The parameters were determined to ensure the well-converged total energies and geometry optimization calculations. The electronic structures were calculated based on the fully relaxed lattice parameters and ionic positions. For the calculation of the electronic and optical properties, a larger 6×6×6 *k*-point set was used.

With respect to the crystal structures of various Bi_2O_3 phases, extensive experimental studies have determined the lattice parameters of unit cells via powder neutron diffraction techniques [28–32]. Here, the unit cells of α-Bi_2O_3, β-Bi_2O_3, and γ-Bi_2O_3 measured by Harwig [28] were used as computational models. While for δ-Bi_2O_3, two crystal structures including Battle [33] and Gattow et al. [34] models were used in consideration of the disorder of oxide ions distributed in the lattice due to the instinct oxygen vacancies. As displayed in Fig. 1, α-Bi_2O_3 and β-Bi_2O_3 have a monoclinic and tetragonal lattice respectively, both containing eight Bi atoms and 12 O atoms per unit cell. Cubic phase γ-Bi_2O_3 has 24 Bi atoms and 36 O atoms. Cubic δ-Bi_2O_3 possesses six O atoms and four Bi atoms both in Battle and Gattow models, whereas the average distributions of six oxygen atoms are at different sites in the lattice.

Results and discussion

Crystal structure

Table 1 lists the relaxed lattice constants together with measured values [28, 33, 34]. It is seen that the optimized parameters of α, β, and γ-Bi_2O_3 are close to the corresponding experimental values. For δ-Bi_2O_3, the simulated lattice constants of Gattow mode are close to the measured data as was

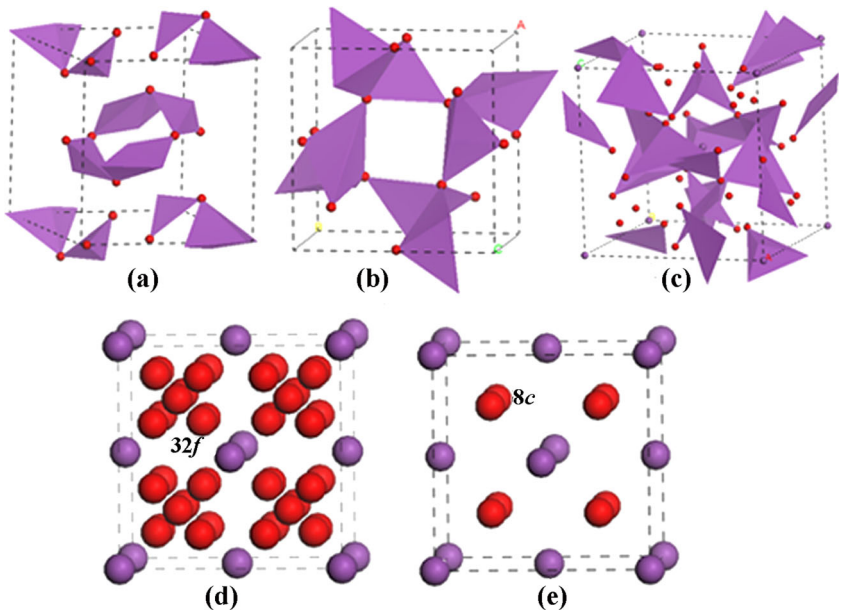

Fig. 1 Bulk structures of α-Bi_2O_3 (**a**), β-Bi_2O_3 (**b**), γ-Bi_2O_3 (**c**), Battle model δ-Bi_2O_3 (**d**): average distribution of six oxygen atoms at the 8*c* (*xxx*, *x*=1/4) and 32*f* (*xxx*, *x*=1/4+δ) sites, and Gattow model δ-Bi_2O_3 (**e**): six oxygen atoms are distributed at the 8*c* site. Red and purple spheres denote the oxygen and bismuth atoms, respectively

Table 1 Relaxed and experimental cell parameters for α, β, γ, and δ-Bi_2O_3[a]. (Lengths in Å and angles in °)

Polymorph	Crystal structure	Space group	Lattice parameters	
α-Bi_2O_3	monoclinic	$P2_1/c$	a=5.849 (5.872)	α=90(90)
			b=8.167 (8.126)	β=112 (113)
			c=7.510 (7.412)	γ=90 (90)
β-Bi_2O_3	tetragonal	P-421c	a=7.948 (7.738)	α=90 (90)
			b=7.948 (7.738)	β=90 (90)
			c=5.602 (5.731)	γ=90 (90)
γ-Bi_2O_3	cubic	I23	a=10.326 (10.250)	α=90 (90)
			b=10.326 (10.250)	β=90 (90)
			c=10.326 (10.250)	γ=90 (90)
δ- Bi_2O_3 (Battle model)	cubic	Fm-3m	a=8.445 (5.648)	α=90 (90)
			b=8.445 (5.648)	β=90 (90)
			c=8.445 (5.648)	γ=90 (90)
δ- Bi_2O_3 (Gattow model)	cubic	Fm-3m	a=5.491 (5.665)	α=90 (90)
			b=5.491 (5.665)	β=90 (90)
			c=5.491 (5.665)	γ=90 (90)

[a] Data in parentheses are experimental values from ref. [28, 33] and [34]

found in the previous study [35]. However, for the Battle model, large lattice distortions were observed, with the unit cell lengths increased by 50 % along a, b, and c directions. Herein, we further investigated the oxygen sublattice in the two models. It is seen from Fig. 1 that the Gattow mode adopts a highly anion-deficient fluorite structure with oxygen occupying 3/4 at the 8c sites of tetrahedral cavities, leaving oxygen with the vacancy of 1/4; while the oxygen also occupies a 32f site in the Battle structure with the vacancy of 17/20. Thus, the oxygen sublattices are spread out within large regions of the tetrahedral cavities, possessing more significant oxygen defect distortions [31, 36]. In addition, it is found in Gattow model that the O−O distance has hardly changed after optimization, whereas the oxygens at 32f sites become more dispersed around the tetrahedral cavities with the O(8c)−O(32f) distance increased by 0.4 Å on average. This in turn results in the large distortions of the crystal structure. The crystal structure of δ-Bi_2O_3 has been the subject of a number of investigations, but there are still lots of conflicts regarding the distribution of oxygen sublattice until now [36–40]. It is recognized that the lattice parameters of the cubic δ-Bi_2O_3 has been correlated with the size of the impurity ions, and δ-Bi_2O_3 transforms to β or γ-Bi_2O_3 phase on cooling from high temperatures to room temperature [18, 41–43]. Since the crystal structure is simulated at 0 K, δ-Bi_2O_3 can be impure with the possible occurrences of intermediate metastable phases and could result in the overestimated unit cell parameters.

Band structures and density of states

It is well acknowledged that the band structures including the valence bands and conduction bands play an important role in affecting the photocatalytic activity of semiconductors. To compare the different electronic structures of α, β, γ, and δ-Bi_2O_3, the band structures and density of states (DOS) are calculated and illustrated in Figs. 2 and 3. Obviously, β-Bi_2O_3 and γ-Bi_2O_3 have direct band gaps and α-Bi_2O_3 has an indirect gap, which is in agreement with experimental observations [22]. The simulated band gaps are 2.23, 1.49, and 2.07 eV for α, β, and γ-Bi_2O_3 respectively, which are smaller than the corresponding measured values 2.8, 2.48, and 2.68 eV [44, 45] due to the well-known band gap underestimation of the DFT theory. However, the character of the band structure and the variation trend of band gaps are expected to be reliable and will not affect the qualitative analysis of the relative energy changes. Moreover, it is worth noting that the band gap of δ-Bi_2O_3 is absent both in the Battle and Gattow models, with conduction bands and valence bands overlapping at the Fermi level. This results in a finite density of states at the Fermi level and a semimetallic character for δ-Bi_2O_3. The same case was also found in the previous theoretical studies [23, 35, 37, 40]. This is usually associated with the underestimation of the forbidden gap in semiconductors in the framework of DFT [25]. Medvedeva et al. used self-interaction corrections in calculations and found the band gap is still absent [37]. However, the forbidden gap appears in a hypothetical bismuth oxide Bi_2O_4, in which both the unit cell vacancies are occupied by the oxygen atoms. Thus, the absence of gap can be associated with the distribution of the oxygen vacancies in the lattice. Conductivity measurements also revealed a finite density of states at the Fermi level [40]. Therefore, δ-Bi_2O_3 has wild applications in electrochemical devices as electrodes owing to its intrinsic oxygen vacancy and high ionic conductivity. In the present study, we focused on the photocatalytic properties of Bi_2O_3, thus the electronic properties of α, β, γ-Bi_2O_3 phases are highlighted to be discussed.

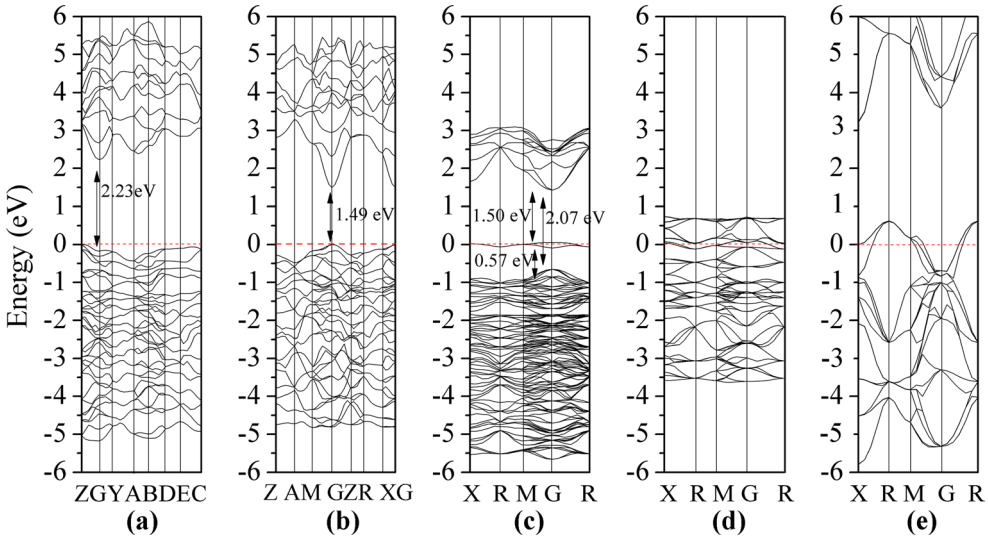

Fig. 2 Band structures of α-Bi_2O_3 (**a**), β-Bi_2O_3 (**b**), γ-Bi_2O_3 (**c**), Battle model of δ-Bi_2O_3 (**d**), and Gattow model (**e**)

Inspection of Figs. 2 and 3, the main features are summarized as follows: (i) For α and β-Bi_2O_3, the top of valence bands are mainly constructed by Bi6s and O2p orbitals, and the bottom of conduction bands is dominantly composed by Bi6p orbital. Therefore, photoelectron mainly transfers from Bi6s and O2p in the top of valence band to Bi6p in the bottom of conduction band. (ii) For γ-Bi_2O_3, the orbital constitution is the same for the frontier bands. One remarkable point is that two intermediate bands are found at the Fermi level, induced by Bi6s and O2p as can be seen in Fig. 3. This leads to two-step transition from the top of valence band to the bottom of conduction band, i.e., the photoelectron fist transits from the top of valence band to intermediate bands and then to the bottom of conduction bands, with transition energies of 0.57 and 1.50 eV, respectively, which are smaller than the direct band gap of 2.07 eV. As a result, electron transition becomes much easier under irradiation, which benefits the enhancement of the visible-light photocatalytic activity as found by experiments [21, 46].

It is known that the separation rate (D) of photogenerated electron (e^-) and hole (h^+) is also a crucial factor for the photocatalytic performance [47, 48]. To analyze the separation rate, we calculated the curvature of the parabolic portions of bands near the top of valence bands and the bottom of conduction bands. A higher D means a lower recombination rate of e^--h^+ pairs. The relationship between the curvature of the bands and the effective mass is shown as follows:

$$m* = \hbar^2 \left(\frac{\partial^2 E}{\partial^2 k} \right)^{-1} = \frac{\hbar^2}{2a} \tag{1}$$

$$D = \frac{a_{CBM}}{a_{VBM}} \tag{2}$$

where m^* is the effective mass of carries and a is the second order coefficient in a quadratic fit of $E(k)$, CBM and VBM denote the top of valence bands and the bottom of conduction bands. Here, a larger value of a corresponds to a lower effective mass of the carriers with a higher mobility. The related results are listed in Table 2. It is noted that β-Bi_2O_3 has the largest a_{CBM} (a_{VBM}), α-Bi_2O_3 the medium and γ-Bi_2O_3 the least, indicating the charge carrier mobility is in the order of $\beta > \alpha > \gamma$. One can also see from the bands fluctuation displayed in Fig. 2, in which CBM and VBM in β-Bi_2O_3 fluctuate highly with wider bands which benefits the carrier

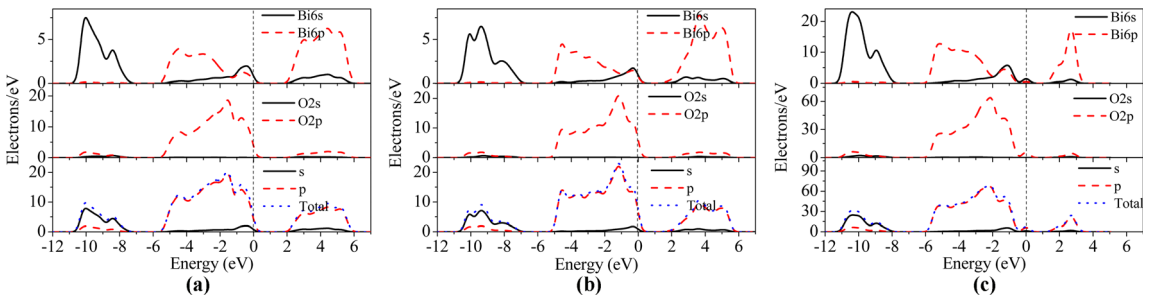

Fig. 3 Total and partial DOS of α-Bi_2O_3 (**a**), β-Bi_2O_3 (**b**), and γ-Bi_2O_3 (**c**)

Table 2 Second-order coefficients in a quadratic fit of CBM/VBM

Crystal	a_{CBM}	a_{VBM}	D
α-Bi_2O_3	54.62	−11.25	4.86
β-Bi_2O_3	96.32	−15.61	6.17
γ-Bi_2O_3	17.13	−7.82	2.19

mobility. In addition, D is also in the sequence of $\beta>\alpha>\gamma$, which means β-Bi_2O_3 exhibits much lower e^--h^+ recombination rates than α-Bi_2O_3 and γ-Bi_2O_3. Considering the electron transition and separation rate of e^--h^+ pair, γ-Bi_2O_3 is still studied as a promising visible-light phtocatalyst although with relatively smaller D value [46].

Optical properties

The interaction of a photon with the electrons can result in transitions between the valence bands and conduction bands. The optical properties can be determined by dielectric function:

$$\alpha(\omega) = \varepsilon_1(\omega) + i\varepsilon_2(\omega) \tag{3}$$

where $\varepsilon_1(\omega)$ and $\varepsilon_2(\omega)$ is the real part and imaginary part of the dielectric function, respectively. $\varepsilon_2(\omega)$ is obtained by the absorption coefficient $\alpha(\omega)$ and the electron energy-loss function $L(\omega)$ can be obtained by the following equations:

$$\alpha(\omega) = \sqrt{2}\omega\left(\sqrt{\varepsilon_1{}^2(\omega) + \varepsilon_2{}^2(\omega)} - \varepsilon_1(\omega)\right)^{1/2} \tag{4}$$

$$L(\omega) = \frac{\varepsilon_2(\omega)}{\varepsilon_1{}^2(\omega) + \varepsilon_2{}^2(\omega)} \tag{5}$$

The absorption coefficient as a function of wavelength is presented in Fig. 4a. The absorption edge locates at about 420, 450, and 550 nm for α-Bi_2O_3, β-Bi_2O_3, and γ-Bi_2O_3 respectively, which means γ-Bi_2O_3 have a wider absorption in the visible-light region and the absorption intensity has the order of $\gamma>\beta>\alpha$ in the visible-light region. To further investigate the optical electron transition, $\varepsilon_2(\omega)$ as a function of energy is plotted in Fig. 4b, which can be obtained from the momentum matrix elements between the occupied and unoccupied wave functions within selection rules. We note that the $\varepsilon_2(\omega)$ curves of α-Bi_2O_3 and β-Bi_2O_3 have similar thresholds of transition, with major peaks at 4.8 eV and 4.5 eV respectively. These peaks mainly come from the electron transitions from the O2p to Bi6p. Another minor and wider peaks at about 13 eV are due to transitions from B6s to Bi6p. Whereas for γ-Bi_2O_3, the major absorption peak locates at about 3.8 eV with a red-shift of 0.7 and 1.0 eV compared to β-Bi_2O_3 and α-Bi_2O_3. This indicates the electron transition needs less energy for γ-Bi_2O_3 which is in agreement with analysis of band structure. Therefore, γ-Bi_2O_3 may exhibit better photocatalytic performance than α-Bi_2O_3 and β-Bi_2O_3 as was found by experiments [46].

The electron energy-loss function $L(\omega)$, an important factor in describing the energy loss of a fast electron traversing a material, is plotted in Fig. 4c. The peaks in $L(\omega)$ represent plasma resonance, and the corresponding frequency is the so-called plasma frequency. It is seen that the variation trend of $L(\omega)$ spectra are very different for α-Bi_2O_3, β-Bi_2O_3, and γ-Bi_2O_3, with the former one exhibiting two comparable broad peaks, and the latter two having one very sharp peak and another broad peak with both peaks shifting to the low energy region. These peaks arise from the electron transitions between Bi6s in the deeper valence bands to Bi6p states. The plasma peaks of β-Bi_2O_3 and γ-Bi_2O_3 both shift to low energy region compared to α-Bi_2O_3. The variation trend is the same with the optical transition spectra.

Conclusions

In this work, we have performed fist-principle calculations on the electronic and optical properties of various Bi_2O_3 polymorphs. The relaxed crystal parameters of α, β, γ, and Gattow mode of δ-Bi_2O_3 were close to the corresponding experimental values. Whereas, large lattice distortions were found for Battle model of δ-Bi_2O_3 due to its large oxygen vacancy. Absent forbidden gap was found in δ-Bi_2O_3, resulting in a

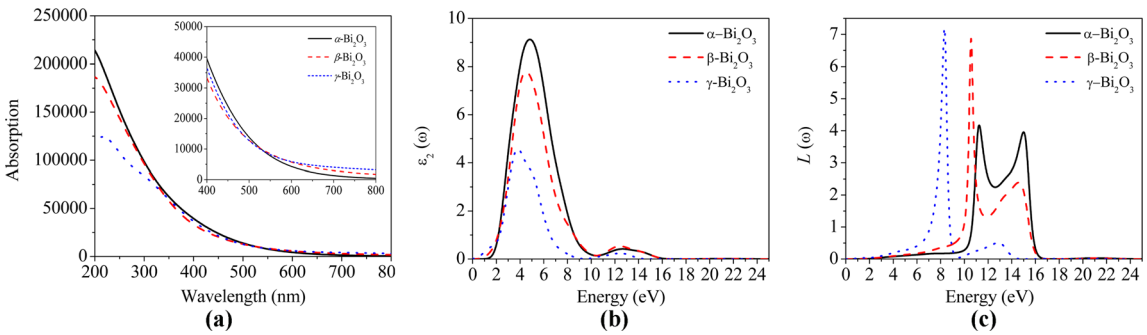

Fig. 4 Absorption spectra (**a**), imaginary part of dielectric functions (**b**), and electron energy-loss functions (**d**) for α-Bi_2O_3, β-Bi_2O_3, and γ-Bi_2O_3

semimetallic character because of its intrinsic oxygen vacancy and high ionic conductivity. For α, β and γ-Bi_2O_3, the top of valence band was constructed by Bi6s and O2p orbitals, and the bottom of conduction band was mainly composed by Bi6p orbital. It was worth noting for γ-Bi_2O_3 that the intermediate bands induced by Bi6s and O2p existed near the Fermi level, which resulted in a two-step transition from the top of valence band to the bottom of conduction band and made electron transition much easier under irradiation. Hence, γ-Bi_2O_3 has been studied as a promising visible-light phtocatalyst although with a relatively smaller e^--h^+ separation rate. This was also supported by the red-shifts of the absorption wavelength in the visible light region and smaller electron transition energy compared to α and β-Bi_2O_3. Therefore, it was concluded that the photocatalytic performance is in the sequence of $\gamma > \beta > \alpha$, which is in accord with experimental observations. The present study promotes the understanding of intrinsic features of Bi_2O_3 polymorphs as promising visible-light photocatalysts.

Acknowledgments We thank the financial support by Sichuan Provincial Education Department Project (No. 14ZB0054), Southwest Petroleum University Fund and Scientific Research Staring Project of SWPU (2013XJZ017, 2014QHZ020, 2014PYZ012).

References

1. Blanco J, Malato S, Fernández-Ibañez P, Alarcón D, Gernjak W, Maldonado MI (2009) Renew Sust Energ Rev 13:1437
2. Kuo TJ, Lin CN, Kuo CL, Huang MH (2007) Chem Mater 19:5143
3. Ren J, Wang W, Shang M, Sun S, Gao E (2011) ACS Appl Mater Interfaces 3:2529
4. Chen X, Mao SS (2007) Chem Rev 107:2891
5. Fujishima A (1972) Nature 238:37
6. Linsebigler AL, Lu G, Yates JT Jr (1995) Chem Rev 95:735
7. Asahi R, Morikawa T, Ohwaki T, Aoki K, Taga Y (2001) Science 293:269
8. Jimmy CY, Wu L, Lin J, Li P, Li Q (2003) Chem Commun 1552
9. Hirai T, Okubo H, Komasawa I (1999) J Phys Chem B 103:4228
10. Kim J, Lee CW, Choi W (2010) Environ Sci Technol 44:6849
11. Hameed A, Gombac V, Montini T, Felisari L, Fornasiero P (2009) Chem Phys Lett 483:254
12. Leontie L, Caraman M, Alexe M, Harnagea C (2002) Surf Sci 507:480
13. Huang CC, Wen TY, Fung KZ (2006) Mater Res Bull 41:110
14. Schröder F, Bagdassarov N, Ritter F, Bayarjargal L (2010) Phase Transit 83:311
15. Drache M, Roussel P, Wignacourt JP (2007) Chem Rev 107:80
16. Laurent K, Wang GY, Tusseau-Nenez S, Leprince-Wang Y (2008) Solid State Ion 178:1735
17. Cornei N, Tancret N, Abraham F, Mentré O (2006) Inorg Chem 45: 4886
18. Sammes NM, Tompsett GA, Näfe H, Aldinger F (1999) J Eur Ceram Soc 19:1801
19. Hameed A, Montini T, Gombac V, Fornasiero P (2008) J Am Chem Soc 130:9658
20. Leontie L, Caraman M, Delibaş M, Rusu GI (2001) Mater Res Bull 36:1629
21. Zou W, Hao WC, Xin X, Wang TM (2009) Chin J Inorg Chem 25: 1971
22. Cheng HF, Huang BB, Lu J, Wang ZY, Xu B, Qin XY, Zhang XY, Dai Y (2010) Phys Chem Chem Phys 12:15468
23. Yin LF, Niu JF, Shen ZY, Sun Y (2011) Sci China Chem 54:180
24. Fischer TH, Almlof J (1992) J Phys Chem 96:9768
25. Perdew JP, Wang Y (1992) Phys Rev B 45:13244
26. Segall MD, Lindan PJD, Probert MJ, Pickard CJ, Hasnip P, Clark SJ, Payne MC (2002) J Phys Condens Matter 14:2717
27. Vanderbilt D (1990) Phys Rev B 41:7892
28. Harwig H (1978) Z Anorg Allg Chem 444:151
29. Blower SK, Greaves C (1988) Acta Crystallogr C 44:587
30. Simonov VI, Kargin YF (1992) Acta Crystallogr B 48:604
31. Yashima M, Ishimura D (2003) Chem Phys Lett 378:395
32. McCabe EE, Jones IP, Zhang D, Hyatt NC, Greaves C (2007) J Mater Chem 17:1193
33. Battle PD, Catlow CRA, Drennan J, Murray AD (1983) J Phys C 16: 561
34. Gattow G, Schroeder H (1978) Z Anorg Allg Chem 444:151
35. Walsh A, Watson GW, Payne DJ, Edgell RG, Guo J, Glans PA, Learmonth T, Smith KE (2006) Phys Rev B 73:235104
36. Mohn CE, Stølen S, Norberg ST, Hull S (2009) Phys Rev B Condens Matter 80:024205
37. Medvedeva NI, Zhukov VP, Gubanov VA, Novikov DL, Klein BM (1996) J Phys Chem Solids 57:1243
38. Aidhy DS, Nino JC, Sinnott SB, Wachsman ED, Phillpot SR (2008) J Am Ceram Soc 91:2349
39. Tanaka I, Togo A, Seko A, Oba F, Koyama Y, Kuwabara A (2010) J Mater Chem 20:10335
40. Carlsson JM, Hellsing B, Domingos HS, Bristowe PD (2002) Phys Rev B 65:205122
41. Schumb WC, Rittner ES (1943) J Am Chem Soc 65:1055
42. Oniyama E, Wahlbeck PG (1998) J Phys Chem B 102:4418
43. Klinkova LA, Nikolaichik VI, Barkovskii NV, Fedotov VK (2007) Russ J Inorg Chem 52:1822
44. Gurunathan K (2004) Int J Hydrog Energy 29:933
45. Hao WC, Gao Y, Jing X, Zou W, Chen Y, Wang TM (2014) J Mater Sci Technol 30:192
46. Sun YY, Wang WZ, Zhang L, Zhang ZJ (2012) Chem Eng J 211–212:161
47. Zhang HJ, Liu L, Zhou Z (2012) RSC Adv 2:9224
48. Ma XC, Dai Y, Guo M, Huang BB (2012) Chem Phys Chem 13:2304